Modeling the Slant Wet Delays From One GPS Receiver as a Series Expansion With Respect to Time and Space: Theory and an Example of Application for the Tahiti Island

Fangzhao Zhang , *Student Member, IEEE*, Jean-Pierre Barriot, Guochang Xu, and Marania Hopuare

Abstract— Traditionally, the modeling of the water vapor contents of the atmosphere is done through the estimation of precipitable water (PW)—the integrated value of the mass of water vapor over a vertical column expressed in millimeter equivalent height. This modeling method is justified by the fact that, to a high degree of approximation, the atmosphere can be seen as the stacking of horizontal layers, including water vapor, over distances larger than the height of the tropopause. Nevertheless, the cycle of the water vapor, the most prevalent of the greenhouse gases in the atmosphere, has a highly turbulent regime both in time and in space that the variations in PW cannot fully embrace. In this article, we explore the modeling method, as a series expansion in time and space, of the slant wet delays (SWDs) from one GPS receiver, as an extension of the usual modeling in zenith wet delays (ZWDs) and then PW values. In the first part, we assess, from a metrological point of view, the derivation of the SWDs computed from GPS carrier phase measurements, in the case of a very humid location, the tropical island of Tahiti, for a typical sample over the wet and dry seasons. In the second part, we introduce the series expansion of the SWDs, as seen from one GPS receiver, in terms of trigonometric functions of time and spherical harmonics of elevation and azimuth. This allows us to infer time and space correlations for the SWDs that are unreachable through the modeling of ZWD values alones. In a third part, to show that our approach also includes the zenith case, we make a comparison between the modeled SWDs in the zenith direction with wind velocities from a ground weather station and radiosonde soundings (RSs). The three main conclusions from our data case are: first, the SWDs are correlated in time by about four days, and in space, with an angular correlation distance of about 20°, both for the dry and wet seasons; second, the postfit residuals are almost uncorrelated with the SWDs from a temporal and spatial point of view, but with a diurnal component; third, there is a weak correlation between the SWDs and wind velocity, the pattern depends on the season.

I. INTRODUCTION

THE water vapor plays an important role in the atmospheric processes. The distribution and variations of atmospheric water vapor are related to the evolution of weather systems, the radiation budget of the climate system, and global warming [1], [2]. Compared with the low-throughput conventional observations, for example, water vapor radiometers (WVRs) and radiosonde soundings (RSs), the ground-based GNSS technology provide high-throughput, all-weather, low-cost observations of the water vapor contents of the atmosphere with high internal repeatability and high accuracy [3]–[6]. However, current GNSS processing provides integrated data over the atmospheric column, in the form of zenith wet delay (ZWD) [and a derived quantity called precipitable water (PW)] and not the underlying 3-D/4-D (time and space) water vapor fields [7].

The use of integrated data over the atmospheric column is mainly based on the fact that the lower atmosphere of the Earth presents, to a large degree of approximation, a layered structure over lateral distances larger than the tropopause altitude with an exponential decay of the pressure with altitude (8.5-km scale height for the Earth). The presence of the atmosphere induces a bending of the radio wave rays (including light), almost only function of the elevation of the ray when it intercepts the Earth's surface, and also induces delays of propagation with respect to vacuum. The bending of light rays is known as astronomical refraction. For radio waves, the bending and the propagation delays are taken into account by the so-called mapping functions that were introduced by the seminal work of Marini (1972) [8]. They were improved year after year, culminating in the family of Vienna-mapping functions [9]. They exist for both zenith total delay (ZTD) and ZWD in a similar fashion. They map the propagation delay along the bended ray to the vertical direction, as seen from the radio wave receiver. They are based on the assumption of a horizontally layered atmosphere. Nevertheless, small variations with respect to the layering exist. First, the layering itself can change as a function of the local values of the temperature

and pressure fields. Some mapping functions take this into account by introducing the surface temperature and pressure of a discretized atmosphere from worldwide databases. Second, small variations of propagation delays are caused by lateral (i.e., nonvertical) variations of the refractivity fields, and are mainly related to the turbulence in the lower troposphere. To deal with these small, but perfectly measurable, lateral variations of the propagation delays, Davis *et al.* [10] introduced, in an empirical way, the so-called horizontal gradients as a sine and cosine functions of the azimuth around the GNSS receiver. This addition is permissible because, when small lateral variations of the refractivity field are introduced, the variations of the bending are of second-order with respect to the first-order variations of the propagation delays [11]. In other words, there is no need in this case to modify the mapping function; the addition of the gradients is sufficient by itself. A straightforward extension should have been to introduce sine and cosine of multiple of the azimuth, as it is done for spherical harmonics. The answer is certainly that the data acquired at this time, both in coverage and accuracy, were insufficient to determine these additional terms. However, we are now 27 years later, with highly precise GNSS orbits, additional constellations of GNSS satellites, and certainly, in the near future, low-Earth orbit GNSS augmented constellations, and this answer is now obsolete.

At the moment, almost all the current GNSS software, that were written with positioning in mind, are outputting, integrated vertical values, like ZTD, ZWD, and gradients, all of them considered as constants for a given time resolution (typically from hourly values to 5-min interval). Therefore, the only path to model the spatiotemporal variations of the water vapor fields is first to reconstruct the slant wet delays (SWDs) from the outputted data, then to use GNSS water vapor tomography [12] based on reconstructed SWDs from a dense ground-based GNSS station network [13], [14]. Numerous efforts have been made to improve GNSS water vapor tomography. Hirahara *et al.* [15] presented a tomographic formulation for determining the local 4-D refractivity distribution in the troposphere above a dense array of GPS receivers using a least-squares scheme. Flores *et al.* [16] also presented a 4-D tropospheric tomography approach based on singular decomposition and Kalman filtering. Bender *et al.* [17] improved GNSS water vapor tomography by combining GPS, GLONASS, and Galileo observations with iterative algebraic reconstruction techniques. Rohm *et al.* [18] investigated 3-D GNSS tomography model using limited constraint and robust Kalman filtering. Zhang *et al.* [19] proposed an improved tomography approach based on adaptive Laplacian smoothing and Helmert variance component estimation. GNSS tomography is a heavy tool to deploy, as it implies a dense network of GNSS stations.

In this article, we propose an intermediate method between the usual ZWD/PW modeling and the full GNSS tomography, based on the rewriting of SWD*sin (elevation) from one GPS station as an expansion in time and space of orthogonal functions. This approach permits to study both the vertical and lateral variations of the water vapor field as seen from one GPS receiver without the complexity of water vapor tomography.

As we have at the moment to use reconstructed SWDs as an intermediate step, we will focus, first, to a metrological study of the reconstruction of these SWDs. In a second part, we will give the mathematical description of our new tool that permits to derive time and space correlations of the water vapor fields as seen from one GPS receiver. In a third part, we will study the correlation to our reconstructed SWDs along the zenith direction (quasi-ZWDs), to illustrate the fact that our algorithm is a generalization of the usual way to monitor ZWD/PW values, and so can handle integrated zenith quantities as a special case. We will illustrate all the computations with the practical example of GPS data acquired from the International GNSS Service (IGS) THTI station over the wet and dry seasons at the Geodesy Observatory of Tahiti (OGT).

II. Estimation of the ZTDs

A. Data Processing

GNSS signals are delayed when they pass through the ionosphere and the neutral atmosphere from a satellite to a ground-based receiver [20]. The ionospheric electron content produces a dispersive delay that can be significantly reduced using dualfrequency combinations [16], [21], [22]. The neutral atmosphere, however, induces an excess delay independent of frequency that can be estimated as a function of the temperature, pressure, and the water vapor contents of the atmospheric layers [5], [23]. The excess delay of the atmosphere is the slant total delay (STD), which sums up the slant hydrostatic delay (SHD) and the slant wet delay (SWD) [24]. The hydrostatic delay, due to the dry gases in the troposphere and the non-dipole component of water vapor, can be precisely modeled based on the surface air pressure and temperature. The wet delay, due to the dipole component of the water vapor, is linked to the partial pressure of the water vapor or equivalently the relative humidity [25]. In the zenith direction, it is named ZTD, and can be divided into two components: the zenith hydrostatic delay (ZHD) and the ZWD (nonhydrostatic) [26].

In this article, we used the Bernese Software Version 5.2 [28] based on the precise point positioning (PPP) approach for the tropical permanent GPS station THTI (Fig. 1, IGS reference name) located in the Central Southern Pacific Ocean [5] to derive the GPS ZTDs during four months in the wet season from November 5, 2017 to March 8, 2018 and four months in the dry season from May 13 to September 15, 2018. Details about our GPS data processing are summarized in Table I.

To validate the quality of our GPS results, we compared our GPS ZTDs with IGS final troposphere products downloaded from the crustal dynamics data information system (CDDIS) archive of GNSS product troposphere files generated by the Jet Propulsion Laboratory (JPL) based on the PPP approach and providing a 5-min resolution (see Table I) [29]. The IGS products based on the Bernese Software Version 5.2 replaced Version 5.0 products from the day of year 29 in 2017. Appendix presents the exact definition of the terms bias, root mean square (rms), and standard deviation (STD).
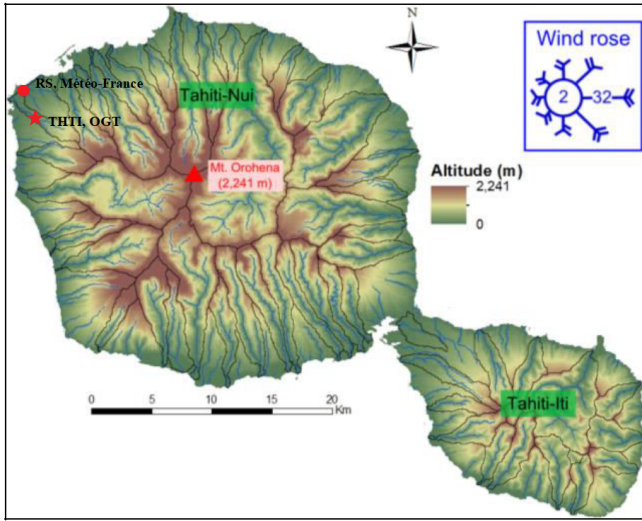
Fig. 1. Location of the THTI GPS station (149.6064°W, 17.5771°S) (red star) and Radiosonde station (149.6145°W, 17.5553°S) (red circle) on the Tahiti Island [27].

TABLE I
CHARACTERISTICS OF OUR GPS DATA PROCESSING
AND IGS DATA ANALYSIS CENTERS

	Our GPS data processing	IGS products
Ephemerides, satellite clocks	CODE final	IGS final
Approach	PPP	PPP
Sampling interval	300 s	300 s
Elevation cut-off angle	3 degrees	7 degrees
Mapping function	Wet VMF1	Wet GMF
A priori ZTD model	ECMWF-based dry VMF1	Global pressure model (GPT)
Ocean loading	Applied	Applied
Atmospheric loading	Applied	Applied
ZTD estimation interval	5 min	5 min

TABLE II
STATISTICAL SUMMARY FOR THE COMPARISON BETWEEN OUR GPS
ZTDs AND IGS ZTDs (IGS MINUS OUR GPS ESTIMATES)
IN TERMS OF MAX, MIN, BIAS, RMS, AND STD

Season	Max (mm)	Min (mm)	Bias (mm)	RMS (mm)	STD (mm)	Data Points
Wet	15.51	−15.54	−0.55	5.19	5.16	35273
Dry	18.02	−18.47	−2.38	5.88	5.38	35749

B. Comparison of Our ZTD Values With the IGS Troposphere Products

In this section, we validate our GPS ZTD values against the IGS ZTD products during the wet season (from November 5, 2017 to March 8, 2018) and the dry season (from May 13 to September 15, 2018). The time resolution of the ZTD is 5 min. Fig. 2 and Table II summarize the results. The ZTD values in the wet season are larger than the ones in the dry season. The distribution of the differences in the wet season is clearly closer to a Gaussian distribution than in the dry season, with no appreciable bias and an rms of 5 mm.

The biases and the rms of the differences between our GPS ZTDs and IGS ZTDs are -0.55 ± 5.19 mm in the wet season and -2.38 ± 5.88 mm in the dry season (Table II). There is a systematic bias, and our GPS ZTDs are always larger than the IGS ZTD for the two seasons. During the dry season, the bias is larger, -2.38 mm. The reasons are probably related to ancillary parameters introduced in the GPS data processing, such as the different cut-off angle and mapping function, and especially weather data, ECMWF-based dry VMF1 versus global pressure model (GPT).

III. DERIVATION OF THE SWDs

A. Data Processing

The ZHDs can be accurately calculated using the Saastamoinen model (1) with an accuracy of 1–2 mm [30]. Then, the ZWDs can be obtained by subtracting ZHDs from ZTDs, as shown in (2)

$$\text{ZHD} = 2.2768 P_s / f(\lambda, H) \qquad (1)$$
$$\text{ZWD} = \text{ZTD} - \text{ZHD} \qquad (2)$$

where $f(\lambda, H) = 1 - 0.00266 \cdot \cos(2\lambda) - 0.00028 \cdot H$, λ(rad) is the station latitude, H(km) is the geoid height in kilometers, and P_s(hPa) is the surface pressure. For the meteorological parameters, we used the data from a rain gauge station which is colocated with the GPS station THTI. The recorded data with 1-min sampling include temperature, relative humidity, pressure, rainfall accumulation, and rainfall intensity [31].

The SWDs, highly variable in space and time, are usually modeled as the ZWDs multiplied by a wet-mapping function $mf_{\text{wet}}(\varepsilon)$ that accounts for the dependence on the elevation, plus horizontal gradients to consider the azimuthal variability of the atmosphere. Our strategy to estimate the SWDs is [32]

$$\text{SWD}_i = mf_{\text{wet}}(\varepsilon_i)[\text{ZWD}_i + \cot(\varepsilon_i)(G_{Ni} \cdot \cos(\theta_i) \\ + G_{Ei} \cdot \sin(\theta_i))] \quad (3)$$

where $i = 1, 2, \ldots, n$. n is the total number of data. ε and θ are the elevation and azimuth angle of a satellite. G_N and G_E are the north and east horizontal gradients from the GPS data processing. Abdel-Monam Younes [33] evaluated the accuracy of 10 wet-mapping functions, and noted that the Saastamoinen mapping function and the Moffet mapping function (4) [34] are able to provide SWD estimates with submillimeter accuracy. In our case, we used the Moffett wet-mapping function because we estimated the SWD values every 5 min. The VMF1/VMF3 family of mapping functions uses meteorological parameters with only a sampling of 6 h [9], [35]

$$mf_{\text{wet}}(\varepsilon) = \frac{1}{\sin(\sqrt{\varepsilon^2 + 2.25^\circ})}. \qquad (4)$$

GPS carrier phase postfit residuals contains all unmodeled tropospheric effects not covered by the estimated tropospheric parameters and other unmodeled effects such as multipath, errors in antenna-phase center variations, or satellite clocks [7], [36]–[38], [43]. Some studies add them to the SWD estimates, but this is controversial as residuals are supposed to be residuals that is showing up no correlation with the SWD
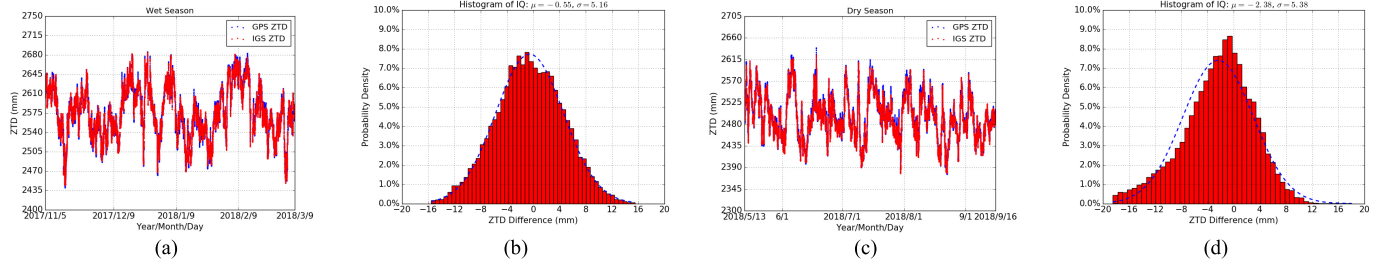
Fig. 2. Comparison of our GPS ZTDs (blue dots) with the IGS ZTDs (red dots) in (a) wet season and (c) dry season, and the ZTD differences between GPS ZTDs and IGS ZTDs in (b) wet season and (d) dry season, with a skewed distribution. The temporal resolution of the ZTD time series is 5 min.
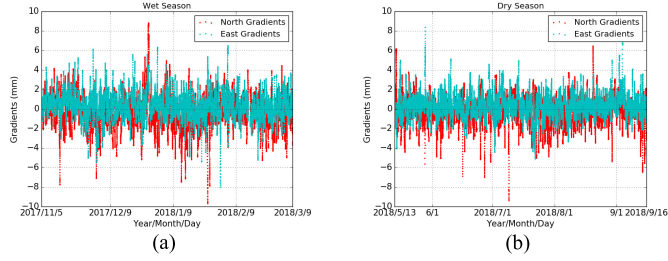

Fig. 3. Variations of the north G_N (red dots) and east G_E (cyan dots) horizontal gradients in (a) wet season and (b) dry season.

Fig. 4. Histograms of the postfit residuals for (a) wet season and (b) dry season, as provided by our GPS data processing.

TABLE III
STATISTICAL SUMMARY FOR THE HORIZONTAL GRADIENTS IN TERMS OF MAX, MIN, MEAN, RMS, AND STD

Gradients	Max (mm)	Min (mm)	Mean (mm)	RMS (mm)	STD (mm)	Data Points
Wet North	8.83	−9.66	−0.30	1.66	1.63	35273
Wet East	6.51	−8.02	0.33	1.36	1.32	35273
Dry North	6.47	−9.37	−0.20	1.38	1.36	35749
Dry East	8.39	−5.10	0.30	1.21	1.18	35749

TABLE IV
STATISTICAL SUMMARY FOR THE POSTFIT RESIDUALS IN TERMS OF MAX, MIN, MEAN, RMS, AND STD, OVER THE WET AND DRY SEASONS

Season	Max (mm)	Min (mm)	Mean (mm)	RMS (mm)	STD (mm)	Data Points
Wet	14.7237	-16.7714	0.0026	1.7365	1.7365	211888
Dry	9.5171	-11.6269	-0.0006	1.5875	1.5875	219976

TABLE V
CORRELATION COEFFICIENTS BETWEEN SWD AND POSTFIT RESIDUALS ALONG THE ZENITH DIRECTION [*sin (ε)] AND ALONG THE SLANT DIRECTION IN THE WET AND DRY SEASONS

Correlation Coefficient		Wet Season	Dry Season
SWD	Residuals	-0.000262	-0.002218
SWD	Residuals *sin(ε)	-0.001469	-0.001316
SWD*sin(ε)	Residuals	-0.010253	-0.007743
SWD*sin(ε)	Residuals *sin(ε)	-0.002670	-0.001107
Data Points		211888	219976

values, or even better, being white noise [40], [41]. In our case, the postfit phase residuals are the zero-differenced residuals based on the PPP approach in our GPS data processing. They have to be transformed into zero-differenced residuals if double-differencing is applied in the GPS data processing [42].

B. Variation of the North and East Horizontal Gradients

In this section, we analyzed the impact of the horizontal gradients on our SWD estimates, which describe the azimuth-dependent part of the neutral atmosphere [43]. The horizontal gradients were estimated during our GPS data processing with the same time interval of 5 min as the ZTD estimates. Fig. 3 shows the variations of the north and east horizontal gradients in the wet season [Fig. 3(a)] and in the dry season [Fig. 3(b)]. Table III summarizes the statistics of the horizontal gradients. It can be noticed that the time variations of the north and east gradients are relatively stable with respect to time, with a mean of about 0.30 mm and an rms of about 1.4 mm. They are not correlated with the geometry of the line-of-sights of the satellites [44].

C. Variation of the Postfit Residuals

The postfit residuals are analyzed from a statistical point of view in this section. We used the Bernese Software Version 5.2
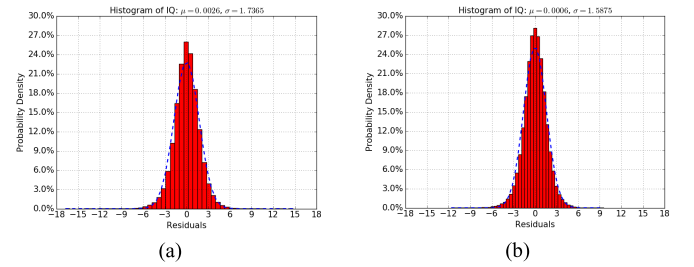
based on the PPP approach to produce the postfit residuals for each satellite. Fig. 4 displays the histograms for all satellites' post-fit residuals in the wet season [Fig. 4(a)] and in the dry season [Fig. 4(b)]. The distributions of the postfit residuals fit Gaussian distributions for the two seasons. The means are at a submillimeter level over the wet and dry seasons (Table IV).

Table V shows the correlation coefficients between the SWD estimates using our strategy (3) and the postfit residuals. All the correlations, slightly negative, are extremely close to zero. This means that the postfit residuals do not contains signal coherent with respect to the SWD estimates. They are all negative because the sign of the sine of the elevation is

always positive; thus, the overall sign of all the four quantities in Table V should be the same.

It can be noticed that the postfit residuals and the application of north and east horizontal gradients in GPS data processing based on Bernese Software Version 5.2 are only minor amplitude components in the derivation of SWDs [41].

IV. ANALYSIS OF THE SPATIAL AND TEMPORAL VARIATIONS OF THE SWDs

A. SWDs as an Approximate Random Function

SWDs are nonrandomly distributed, as they strongly depend on the elevation of the line-of-sight between a ground-based receiver and a GNSS satellite, because of the layering of the Earth atmosphere. As almost all statistical analysis tools refer to stationary functions [45], [46], we translated the modeled SWDs to an almost stationary process with respect to the elevation ε (i.e., independent or quasi-independent of elevation) by considering the quantity

$$SE = SWD * \sin(\varepsilon). \tag{5}$$

The key difference between the sine of the elevation in (5) and a full mapping function is that the sine term does not contain any assumption or information about the fine underlying structure of the atmosphere. This approach was first used by Schön and Brunner [46] and Vennebusch et al. [47] in their studies of the SWDs. For the general setup about the modeling of phase and amplitude fluctuations imposed on signals that travel through the atmosphere, it must be stressed that the SE is not stationary in time, because it is affected by seasonal signals and trends [48]. Another possibility to convert the SWDs to an almost stationary process with respect to elevation could have been to subtract from the observed SWDs the theoretical SWDs computed from a standard model of the atmosphere. This is done in GPS positioning, where the ellipsoidal heights are relative to a standard Earth given by a reference ellipsoid (almost always the WGS84 model). This implies some arbitrariness in the choice of the standard atmosphere. In this article, we used the approach outlined in (5).

Another important fact to consider when we deal with the line-of-sight (slant) directions is their pattern in the sky. Twenty GPS satellites are visible from the THTI station every day, with each satellite following almost the same track in the sky (Fig. 5). This pattern is important because it essentially limits the spatial resolution of the water vapor field in the atmosphere as seen from the THTI station.

B. Least-Squares Fit of the SWDs

To be able to manage a second-order analysis of the SWDs in the statistical sense, we did a least-squares fit of the SE values. For this purpose, we wrote SE as a function of time (t), elevation (ε) and azimuth (a), as seen from the GPS receiver (THTI in our case), as

$$SE(t, \varepsilon, a) = \sum_{n=0}^{N} \sum_{l,m=0}^{L} C_{n,l,m} P_n(t) Y_{l,m}(\varepsilon, a) \tag{6}$$

where the $P_n(t)$ are orthonormal functions, and the $Y_{l,m}$ are spherical harmonics functions. We have to emphasize that
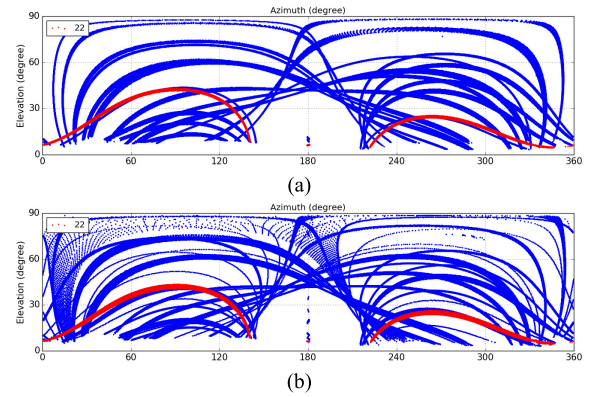

Fig. 5. Sky tracks (in elevation and azimuth) of the GPS satellites visible from the THTI station, in (a) wet season and (b) dry season. The red dots present the sky track of GPS satellite 22, which presents a good coverage in longitude.

SE is only defined on a hemisphere (the sky as seen from the GPS receiver), not the whole sphere. A summary about modeling data over a hemisphere can be found in Ellsaesser [49], Gautron et al. [50], and Huang et al. [51]. The key point to understand about this representation, once the coefficients $C_{n,l,m}$ are determined through a least-squares process, is that by fixing ε and a to a priori values, we can get a time series along any given direction (including the zenith with $\varepsilon = \pi/2$). We can get a sky map by fixing t, at time t, of SE over the hemisphere centered at the GPS station. The coefficients $C_{n,l,m}$ contain all the physical information, on the contrary to the representation in terms of mapping functions/gradients that does not allow a second-order statistical analysis.

Then, we can analyze these time series using the autocovariance and time structure functions, and the maps, at any given time t, using isotropic spatial covariance analysis [52]. In this case, isotropy means that the spatial covariance function between two points in the sky only depends on the spherical distance, as seen from the receiver, between these two points. If SE was known over the whole sphere, the isotropic covariance function at a given time t could be written as Legendre series of the spherical distance ψ as in geoscience fields [52]. But SE is defined only over a hemisphere, thus we cannot build the isotropic covariance in this way. Another possibility is to assume that SE is an even function of elevation when the elevation is negative, but this is just a mathematical trick without a physical basis. Furthermore, in practical cases, low elevation observations are usually outliers that are rejected in GPS processing, so we will get almost no coverage near the equator of the sphere. Therefore, in this article, we revert to the basic definition of the isotropic spatial covariance function (with $t = t_F$ fixed), as in [52]

$$Cov(t_F, \psi) = \int_{a=0}^{a=2\pi} \int_{\varepsilon=-\pi/2}^{\varepsilon=\pi/2} \int_{\alpha=0}^{\alpha=2\pi}$$
$$\times SE(t_F, \varepsilon, a) SE(t_F, \varepsilon', a') \cos(\varepsilon) d\varepsilon da d\alpha \tag{7}$$

where the elevation ε' and azimuth a' are understood to be related to elevation ε and azimuth a by

$$\cos(\psi) = \cos(\varepsilon) \cos(\varepsilon') + \sin(\varepsilon) \sin(\varepsilon') \cos(a - a'). \tag{8}$$

To apply it to our case, we limited it to a half-sphere as

$$\text{Cov}(t_F, \psi) = \int_{a=0}^{a=2\pi} \int_{\varepsilon=0}^{\varepsilon=\pi/2} \int_{a=0}^{a=2\pi}$$
$$\text{SE}(t_F, \varepsilon, a)\text{SE}(t_F, \varepsilon', a')\cos(\varepsilon)d\varepsilon da d\alpha. \quad (9)$$

The covariance function is characterized by its correlation length, which is defined as the value of the argument ψ for which the covariance function has decreased to half of its value at $\psi = 0$ [53].

If we fix, after the determination of the $C_{n,l,m}$ coefficients, the elevation ε and azimuth a to the fixed values ε_F and a_F, we get a time series SL as

$$\text{SL}(t) = \sum_{n=0}^{N} \sum_{l,m=0}^{L} C_{n,l,m} P_n(t) Y_{l,m}(\varepsilon_F, a_F). \quad (10)$$

In this article, the structure function was used to analyze time series, as introduced by Kolmogorov [54], who used it to model turbulence, followed by Tatarski [55], and which is now used in many fields of geosciences [56]. The structure function is less sensitive to biases and trends in SL than the autocovariance function [57]. Dodson *et al.* [58] used the structure functions to represent the fluctuations of the ZWD. Ruf and Beus [59] obtained in this way additional information about the vertical distribution of water vapor in the boundary layer from the turbulence structure of integrated water vapor.

Mathematically, the structure function is defined as

$$S(\tau) = \frac{1}{T} \int_{t=t_0}^{t=t_0+T} [\text{SL}(t) - \text{SL}(t+\tau)]^2 dt \quad (11)$$

where T is infinite [45]. For a finite T, there is two ways to define the structure function. The first is to assume that SL is zero outside the integration interval. This is equivalent to this definition [60]

$$S(\tau) = \frac{1}{T} \int_{t=t_0}^{t=t_0+T-\tau} [\text{SL}(t) - \text{SL}(t+\tau)]^2 dt. \quad (12)$$

The second possibility is to assume that SL is periodic with a period of T. This is a better assumption, from a physical point of view, because SL is a random function that should look always "the same." From a pragmatic point of view, the two definitions give similar results when τ is sufficiently small. In our case, we limited τ to be less than 10 days, that is the residence time of water in the atmosphere [45]. The structure function can also be characterized by a correlation length, as an extension of the notion of correlation length for the covariance function. The basis for such an extension is that for a purely stationary random function, the structure function reduces to the opposite of a covariance function [50]. The definition of the correlation length is therefore the same as the one for the covariance function, but applied to the opposite of the structure function.

For the functions in time $P_n(t)$ in (6), we studied three distinct possibilities: 1) usual sine and cosine functions; 2) Chebyshev polynomials; and 3) Haar wavelets. In the trigonometric series approximation, the average error (in the

least-squares sense) is minimized [61]. In the Chebyshev approximation, the average error can be large but the maximum error is minimized [61], generally at the expense of spurious oscillations at the beginning and end of the defined interval (edge effects), that can also exist to a lesser extent in trigonometric series. The Chebyshev polynomials are the most popular general basis functions used in spectral methods [62]. The Haar wavelet [63] is the first and simplest orthonormal wavelet basis, and does not involve, like other wavelet families, the introduction of additional parameters [64].

A careful examination of the least-squares fit of (6) showed that the edge effects of Chebyshev polynomials were large, as expected, at the beginning and end of the time series, and that sine/cosine function and Haar wavelets presented almost identical results. For simplicity, we retained the sine/cosine pairs as our representation of the time variations.

V. RESULTS AND DISCUSSION

A. Fits of the SWDs for the Wet and Dry Seasons

In this section, we used two sets of four-month data, one acquired during the dry season from November 5, 2017 to March 8, 2018, the other one acquired during the wet season from May 13 to September 15, 2018. We were able to obtain a resolution in time down to almost diurnal variations, with $N = 385$ ($2n + 1$ coefficients for the sine/cosine expansion in time). The maximum degree and order of the spherical harmonic expansion was pushed to $L = 6$, corresponding to a resolution of about 30° in spherical distance in the sky. This limitation is probably driven by the pattern of the sky tracks of the GPS satellites (Fig. 5). We dealt with two kinds of signals: the first one was SE, as defined by (5), and the second one was PFR*sin (ε) (or PFRE), where PFR are the postfit residuals. Above these limits on N and L, the condition numbers of the least-squares normal matrices rapidly degraded, with nonphysical large oscillations in the solution. The results of the fits are shown in Figs. 6 and 7.

The GPS satellite number 22 (Fig. 5) was chosen to illustrate the fit of the SE signals and PFRE signals along its sky track. Fig. 7 shows the fits of SE signals and PFRE signals along the sky track of GPS satellite number 22 for the wet season and the dry season. The fit is almost perfect for the SE signal, but not for the PFRE signal.

Fig. 8 shows the SE and PFRE signals calculated in the zenith direction during the wet and dry seasons. This zenith direction does not correspond to any actual satellite position. The diurnal feature can be seen on the PFRE signal, probably due to aliasing caused by the limit $N = 385$, since the PFRE signal contains more power than the SE signal at high frequencies. The amplitude of the PFRE signal is approximately 8 mm compared to the 250-mm amplitude of the SE signal. According to Figs. 6–8, it is clear that the SE signals are completely fitted by (6). The PFRE signal appears as colored noise, which is just to say that is not a pure white noise, with some signal structure superimposed on diurnal variations, as shown in Fig. 8(b) and (d). Fig. 9 shows the sky view of the SE and PFRE signals at the middle of the time interval for
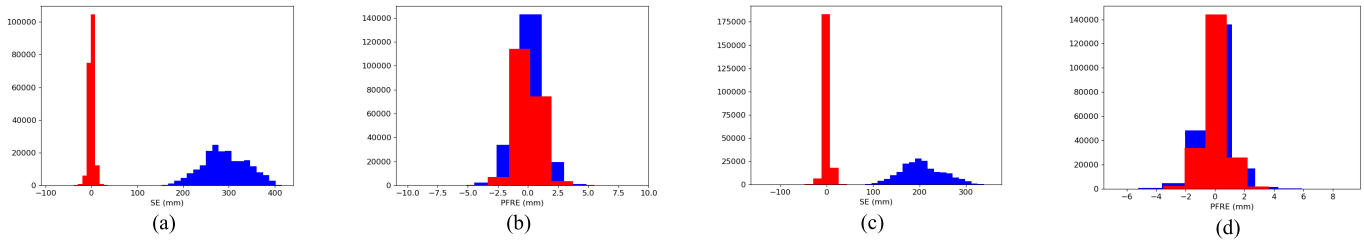
Fig. 6.   Histograms of the fits of the SE signals for (a) wet season and (c) dry season, and histograms of the fits of the PFRE signals for (b) wet season and (d) dry season. (Blue denotes the prefit (i.e., the histogram of the data themselves) and red denotes the postfit residuals.) The SE signal is well fitted to the contrary of the PFRE signal.
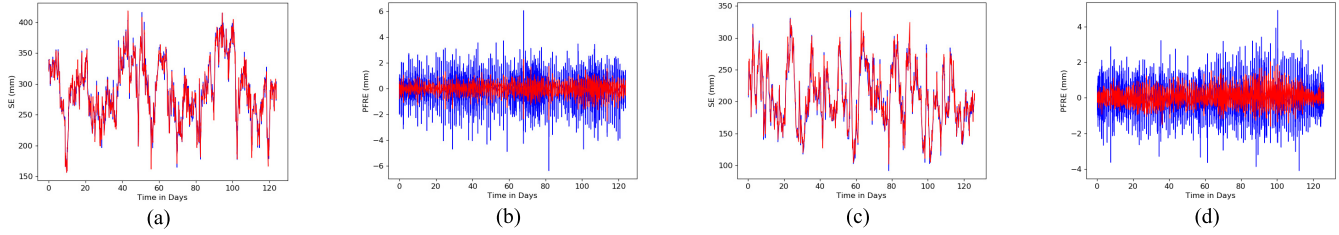

Fig. 7.   Fits of the SE signals along the sky track of GPS satellite number 22 (see sky track in Fig. 5) for (a) wet season (a) and (c) dry season, and the same fits for the PFRE signals for (b) wet season and (d) dry season. [Blue denotes data sets and red denotes the fit through (6).] The SE signal is well fitted to the contrary of the PFRE signal.
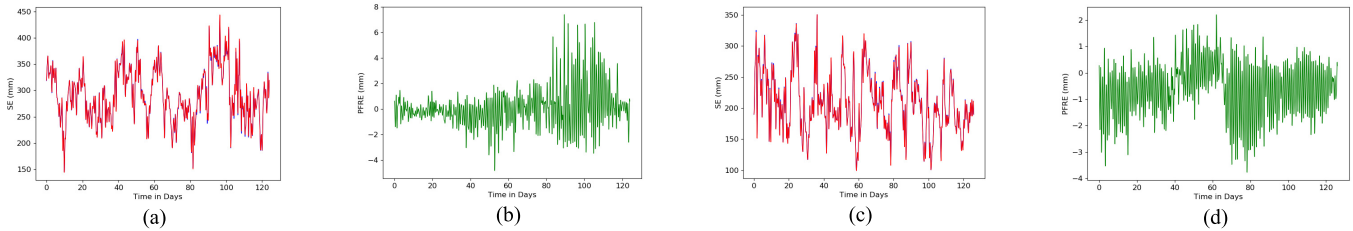

Fig. 8.   SE signals on the zenith direction (red) for (a) wet season and (c) dry season, and PFRE signals on the zenith direction (green) for (b) wet season and (d) dry season, as computed from (6). (Blue denotes SE and PFRE signals.).

the wet season (124 days) and for the dry season (126 days). The variations of SE values and PFRE values are consistent with respect to the spatial mean values at this specific time (Fig. 7). For the wet season, the fluctuations of the SE values and PFRE values are larger than in the dry season. Meanwhile, the absolute PFRE values are large when the elevation angle is near 0° and 90° [Fig. 9(b) and (d)].

The logarithms of the structure functions, with respect to the two definitions, for the SE and PFRE signals on the zenith direction, over ten days, are shown in Fig. 10(a) and (c) (wet season) and in Fig. 11(a) and (c) (dry season). The main result is that the SE signals are correlated in time by about four days, and that the PRFE signals show a diurnal signature.

In our case, the isotropic spatial covariance function has to restrict to the half-sphere that is the sky as seen from the GPS receiver. The modeled time-averaged covariance function of the SE and PFRE signals is shown in Fig. 10(b) and (d) (wet season) and in Fig. 11(b) and (d) (dry season). The correlation length is around 20° for both the SE and PFRE signals for the two seasons. These correlation lengths, both in time and space, are probably related to the size and time evolution of small-scale atmospheric eddies [65], but this is outside the scope of this article.

B. Correlation Between SE and Wind Velocity

In this section, we investigated the impact of the wind velocity on the SE values. Two kinds of wind data sets were considered: the first one is the local "ground" wind data with an hourly resolution retrieved from the National Oceanic and Atmospheric Administration (NOAA) (ftp.ncdc.noaa.gov), collected on a 10-m mast located at the weather station (TAHITI-Faa'a, about 3 km from our GPS THTI station), the second wind data set is from radio soundings (1000 and 2500 m) with twice a day launches (00:00 UTC and 12:00 UTC), from the same weather station.

Wind flow over the Island of Tahiti is stirred by two main anticyclones. The one is a steady tropical anticyclone centered on the Easter Island (110°W, 28°S), which creates strong and warm trade winds in the east/north-east direction on Tahiti (sometimes in the south-east direction, especially during austral winter). The other is a semipermanent subtropical anticyclone centered on the Kermadec Islands (180°W, 30°S), which moves from west to east and creates cooler trade winds in the south-east direction on Tahiti Island.

Following the apparent position of the sun, the centers of both anticyclones move with the annual cycle: during austral winter, both anticyclones move northwards, while they move
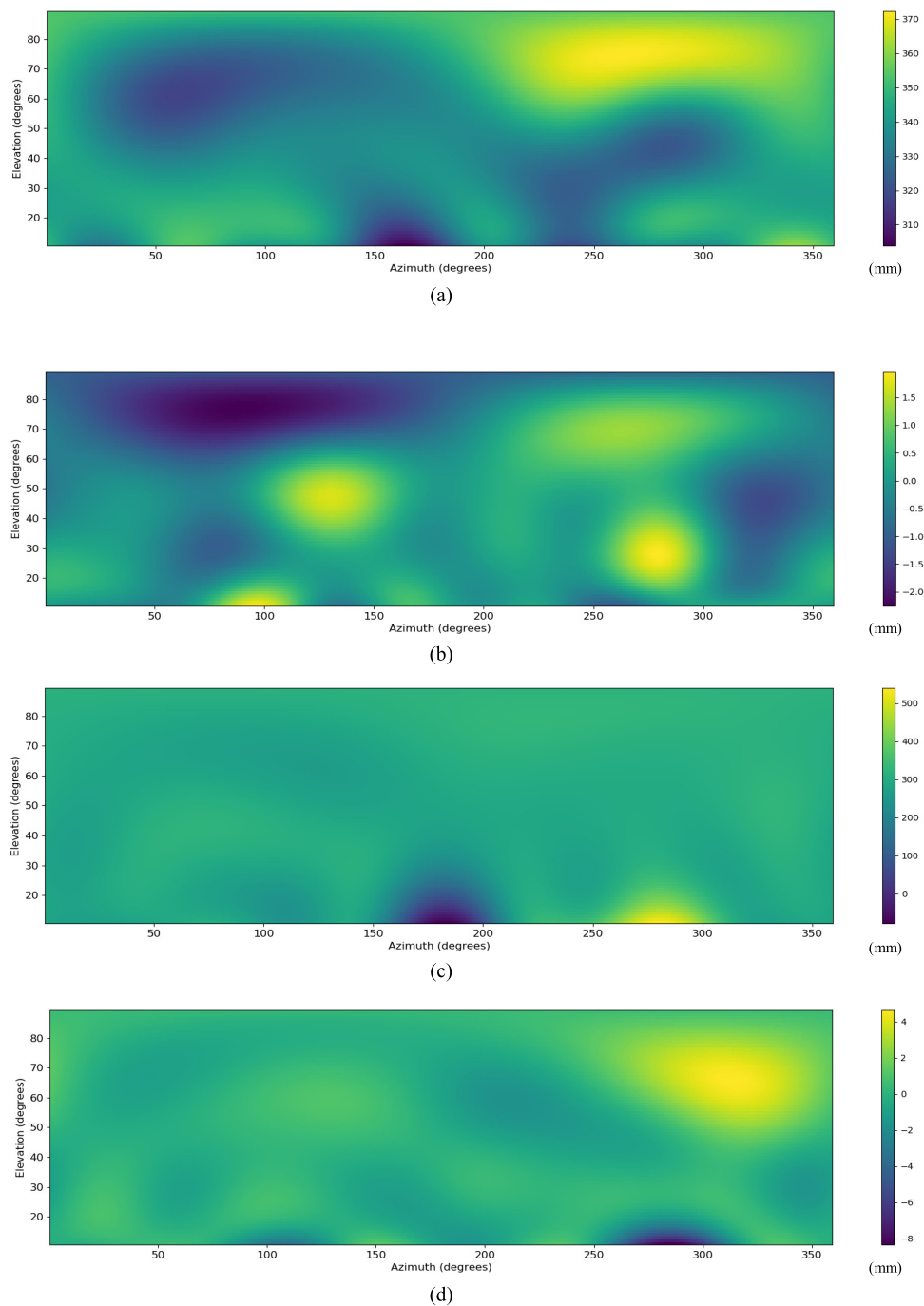
Fig. 9. Sky view of (a) SE signals and (b) PFRE signals at the middle of the time interval (124 days) for the wet season, and sky view of (c) SE signals and (d) PFRE signals at the middle of the time interval (126 days) for the dry season. (Colorbar: the variations of SE values and PFRE values in mm.).

southwards during austral summer; during austral summer, cool trade winds blow on warm water, which creates a thick unstable layer, from the ocean surface up to 5000-m altitude. Only low- or mid-level cumulus clouds develop. Trade winds can also drag organized convective structures from the Easter Island high pressure center, generating multiday bad weather episodes over Tahiti. During austral winter, winds are mostly coming from the Kermadec anticyclone, and carry less moisture. The trade wind layer is more stable and thinner (about 1500 m thick), with fewer clouds and less bad weather

structures [66]. A wind regime, known as the "Mara'amu," can occur in winter: strong trade winds, coming from the Kermadec anticyclone, blows from the south-east direction.

Fig. 12 shows the time series of wind velocity from the weather station at 10 m (boundary layer, blue line, and sampling time 1 h) and from RS data at 1000 m (red line, twice per day) and at 2500 m (green line, twice per day), for the wet season [Fig. 12(a)] and for the dry season [Fig. 12(b)]. From the basic statistics of Table VI, it can be noticed that the wind velocity, essentially horizontal, is increasing, in the
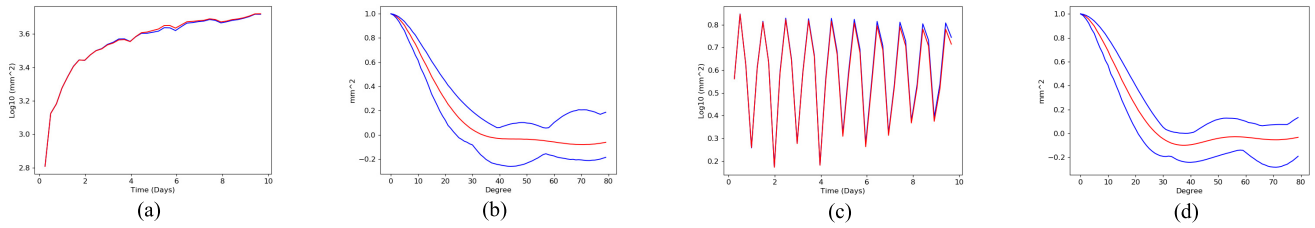
Fig. 10. Log10 of the structure function over ten days corresponding to (a) SE and (c) PFRE on the zenith direction (*Y*-axis) (red: signal strictly limited to the interval of definition, blue: signal assumed to be periodic outside the interval of definition), and covariance function of the spatial repartition of the water vapor to (b) SE and (d) PFRE (*Y*-axis) (red: covariance function as a function of the spatial separation in degrees averaged over the whole dry season, blue: min and max of the covariance function, that is a function of time, over the wet season).
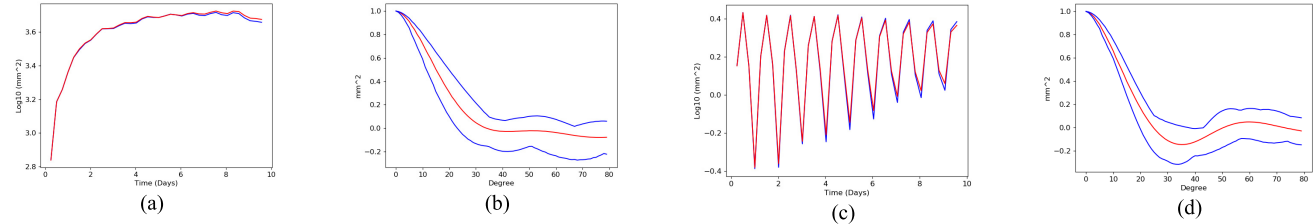

Fig. 11. Log10 of the structure function over ten days corresponding to (a) SE and (c) PFRE on the zenith direction (*Y*-axis) (red: signal strictly limited to the interval of definition, blue: signal assumed to be periodic outside the interval of definition), and covariance function of the spatial repartition of the water vapor to (b) SE and (d) PFRE (*Y*-axis) (red: covariance function as a function of the spatial separation in degrees averaged over the whole dry season, blue: min and max of the covariance function, that is also a function of time, over the dry season).
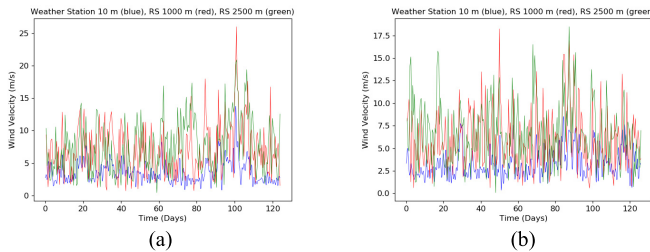

Fig. 12. Wind velocity from the weather station at Faaʻa (about 3 km from our GPS station), at a/10 m (blue, sampling time one hour), b/1000 m (red, from RS balloon, twice per day), c/2500 m (green, from RS balloon, twice per day) for (a) wet season and (b) dry season.

TABLE VI

BASIC STATISTICS FOR THE WET SEASON AND DRY SEASON (FOUR MONTHS). THE FIRST THREE TIME SERIES HAVE BEEN FILTERED DOWN TO TWO SAMPLES PER DAY, THE RESOLUTION OF THE RADIOSONDE MEASUREMENTS OF THE WIND (1000- AND 2500-m ALTITUDES)

	Wet season		Dry season	
	Mean	Deviation	Mean	Deviation
SE zenith delay	291.0 mm	47.24 mm	209.6 mm	45.06 mm
SE time derivative	−0.3941 mm/day	61.57 mm/day	−0.3446 mm/day	64.94 mm/day
Wind 10 m	3.306 m/s	1.118 m/s	2.501 m/s	0.7801 m/s
Wind 1,000 m	7.039 m/s	3.409 m/s	5.939 m/s	2.736 m/s
Wind 2,500 m	7.624 m/s	3.742 m/s	6.685 m/s	3.114 m/s

TABLE VII

CORRELATIONS BETWEEN SE ZENITHAL DELAYS AND SE ZENITHAL TIME DELAYS DERIVATIVE WITH WIND VELOCITY FOR THE WET SEASON AND DRY SEASON, ACCORDING TO TABLE VI STATISTICS

Wind	Wet season		Dry season	
	SE zenithal delay	SE time derivative	SE zenithal delay	SE time derivative
10 m	0.0912	0.0016	0.2066	0.0002
1,000 m	0.2216	− 0.0445	0.1013	−0.0282
2,500 m	0.2028	−0.1373	−0.0137	0.0417

mean, with altitude, but with large deviations from this rule of thumb for the wet and dry seasons.

Fig. 13 shows the correlation between the SE zenith delay and the wind at the altitude of 1000 m and the correlation between the SE zenith delay time derivative and the wind

at the altitude of 2500 m. According to the basic statistics of Table VI, Table VII shows that the correlation coefficient between the SE zenith delay and the wind at the altitude of 1000 m is 0.2216 for the wet season and 0.1013 for the dry season, and the correlation coefficient between the SE zenith delay time derivative and the wind at the altitude of 2500 m is −0.1373 for the wet season and 0.0417 for the dry season. There is a weak correlation between SE and wind velocity during the wet season that is not apparent during the dry season.

Table VII shows very weak correlation coefficients between SE zenith delays and wind velocities. The correlation is the lowest in the dry season between 2500-m wind speed and SE zenith delays. This could be explained by the fact that the trade wind's layer is thinner during the dry season, and it is approximately 1500 m thick during the dry season. Therefore, the correlation breaks down. The weak correlation could be explained by the fact that SE zenith delays represent the sum of two sources of water vapor: evaporation and water vapor blown by the trade winds. If we look at the 1000-m-height
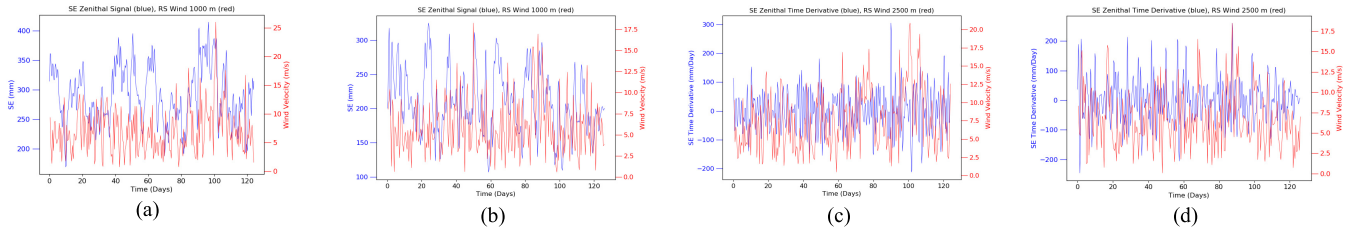
Fig. 13. Visual correlation between the SE zenith delay and the wind at 1000-m altitude for (a) wet season and (b) dry season, and correlation between the SE zenith delay time derivative and the wind at 2500-m altitude for (c) wet season and (d) dry season.

wind, it seems that SE zenith delays increases with increasing wind velocity during both dry and wet seasons. There is a weak but positive correlation. Water vapor coming from the ocean evaporation around Tahiti does not substantially vary between austral summer and winter (sea surface temperature variation), but the trade winds are known to drag more humidity during the wet season than during the dry season. In the wet season, the advection of moist air parcels is high: in the SE zenith delays, advection dominates evaporation. In the dry season, the trade winds are drier. Hence, they enhance evaporation around Tahiti: evaporation dominates advection in the SE zenith delays. Laurent *et al.* [66] provided evaporation data from the local station of Faa'a (about 3 km from the GPS station) that confirm the low values (evaporation of 105 mm/month) in January (wet season) and high values (164 mm/month) in July (dry season).

To summarize, our results show weak but positive correlation between SE zenith delays and 1000-m-altitude wind speed in both seasons. Indeed, during the wet season, the increased advection of moist air leads to a rise of SE zenith delays and during the dry season, the increased evaporation due to drier trade winds also leads to a rise of SE zenith delays. This is confirmed by the positive correlation coefficients with the 1000-m wind in each season. Decomposing the SE zenith delays in advection and evaporation terms is beyond the scope of this article, and only a microscale meteorological model of Tahiti Island will be able to further investigate this topic.

VI. CONCLUSION

In this article, we analyzed, from a metrological and statistical point of view, the SWD estimates computed from GPS carrier phase measurements, on the tropical island of Tahiti, located in a very humid zone. The work was divided in two parts. In the first metrological part, for two data sets spanning the wet season from November 5, 2017 to March 8, 2018 and the dry season from May 13, 2018 to September 15, 2018, we estimated the ZTDs using the Bernese Software Version 5.2 with the PPP approach and the VMF1 mapping function, and evaluated the accuracy of our GPS ZTD estimates by comparing with the IGS final products. The ZWD estimates were obtained by subtracting the ZHDs from the ZTDs, with the ZHDs calculated using Saastamoinen model [30]. The SWDs were estimated with a temporal resolution of 5 min, through the Moffet wet mapping function [34], complemented with horizontal gradients, and without the addition of postfit residuals. The effect of the

inclusion on our SWD estimates of the horizontal gradients and the postfit residuals was investigated. In our case, the postfit residuals seem to be mainly a colored noise showing no correlation with the SWDs.

In a second part, we studied, from a statistical point of view, the two sets of SWDs for the wet and dry seasons derived in the first part. To have stationary or almost stationary signals with respect to space, we studied, according to Schön and Brunner [46] and Vennebusch *et al.* [47], the quantities SWD*sin(elevation). To derive second-order statistics, we fitted these quantities, in a least-squares sense, by a series expansion in time (sine and cosine functions) and space (spherical harmonics). We were able to push the expansion up to nearly diurnal variations in time and 30° in angular separation. As the fitted quantities are nonstationary with respect to time, we used a structure-function approach, less sensitive to trends and periodic signatures to derive the correlation length in time that was found to be around four days. The corresponding postfit residuals are showing up a diurnal signature. A covariance approach was retained for the variations with respect to time. The mean, time-averaged covariance length is around 20° for both the SWD and postfit residuals related quantities, for both seasons.

Besides, we investigated the relationship between SE values and wind velocity measurements. Only the correlation with 1000-m wind speed gave reliable information. Indeed, 10-m wind speed is too close to the surface where turbulence is important, while 2500-m wind speed is too high during the dry season. In both seasons, correlation is positive between SE and the 1000-m wind speed. In the wet season, wetter trade winds drag moist air parcels. As the advection of water vapor increases, the SE values also increases. In the dry season, the drier trade winds allow more evaporation around Tahiti, which contributes to a rise of SE values. These assumptions need to be further investigated through the use of microscale meteorological simulations.

Is the approach developed in this article directly implementable in GNSS software, as a replacement of the mapping functions complemented by gradients? The response is a careful yes. Strictly speaking, a mapping function defines, from the point of view of differential geometry, a coordinate chart that is a nonorthogonal system of coordinates made of the refracted elevation, the length along the bended ray, and the azimuth. Besides, this coordinate chart may evolve with time as a complex function of weather parameters (for example, the VMF1 mapping function). In such a complex, evolving

system of coordinates, defining second-order quantities like structure/covariance functions is almost impossible, as these functions will mix the propagation medium properties with the underlying geometry of the coordinate chart. It is the opinion of the authors that such an implementation in GNSS software implies at least the use of a constant (i.e., not evolving with time) system of coordinates (i.e., a constant mapping function), that therefore must be computed with respect to some standard model of the atmosphere, carefully designed and normalized. The approach developed in this article can be seen as an intermediate step.

The limitation of this article in terms of spatial and temporal resolution is only due to the fact that only 4 to 12 GPS satellites can be observed from one given site (over 32). In the near future, more than 120 GNSS satellites from different constellations will be available [44], multiplying the observable line-of-sights by a factor between 2 to 4 from a given location. This improved coverage will allow the imaging of the water vapor fields by our method with a temporal resolution of a few minutes and a spatial resolution of $10°$ or less.

Finally, the modeling method of SWDs through an expansion series in time and space [see (6)] can be also used to model tropospheric delays, in a correlated way, between uplink and downlink signals to planetary space crafts, where the uplink and downlink separation in time can reach tens of minutes or even hours [67], [68].

APPENDIX

We calculated the correlation coefficients between two variables (SWD and postfit residuals) in the zenith direction and in the slant direction using the correlation formula [5], as

$$r(X, Y) = \frac{\text{covariance}(X, Y)}{\sigma_X \sigma_Y}. \quad (13)$$

The covariance function is

$$\text{covariance}(X, Y) = \frac{\sum_{i=1}^{n} (X_i - \acute{X})(Y_i - \acute{Y})}{n - 1} \quad (14)$$

where $r(X, Y)$ denotes the correlation between the variables X and Y; in our case, we analyzed the correlation between X [SWD or SWD*$\sin(\varepsilon)$] and Y [residuals or residuals*$\sin(\varepsilon)$]. σ_X and σ_Y are the standard deviation of the variables X and Y. $\acute{X}$ and $\acute{Y}$ denote the mean value of X and Y, $i = 1, 2, \ldots, n$. n is the total number of data points.

The statistical summary [bias, rms and standard deviation (STD)] between our GPS results and reference data are given. The bias, rms, and STD parameters are calculated as shown [5]

$$\text{Bias} = \frac{1}{n} \sum_{i=1}^{n} (G_i - R_i) \quad (15)$$

$$\text{rms} = \sqrt{\frac{1}{n} \sum_{i=1}^{n} (G_i - R_i)^2} \quad (16)$$

$$\text{STD} = \sqrt{\frac{1}{n} \sum_{i=1}^{n} ((G_i - R_i) - \text{Bias})^2} \quad (17)$$

where $i = 1, 2, 3, \ldots n$. n denotes the total number of data points. In this case, G denotes our results from our GPS data processing and R is the reference data.

REFERENCES

[1] J. Liu, "Precipitable water vapor on the Tibetan plateau estimated by GPS, water vapor radiometer, radiosonde, and numerical weather prediction analysis and its impact on the radiation budget," *J. Geophys. Res.*, vol. 110, no. D17, 2005, Art. no. D17106.

[2] X. Wang *et al.*, "Tropospheric wet refractivity tomography based on the BeiDou satellite system," *Adv. Atmos. Sci.*, vol. 31, no. 2, pp. 355–362, Mar. 2014.

[3] M. Bevis, S. Businger, T. A. Herring, C. Rocken, R. A. Anthes, and R. H. Ware, "GPS meteorology: Remote sensing of atmospheric water vapor using the global positioning system," *J. Geophys. Res.*, vol. 97, no. D14, p. 15787, 1992.

[4] Z. Baldysz, G. Nykiel, M. Figurski, and A. Araszkiewicz, "Assessment of the impact of GNSS processing strategies on the long-term parameters of 20 years IWV time series," *Remote Sens.*, vol. 10, no. 4, p. 496, Mar. 2018.

[5] F. Zhang, J.-P. Barriot, G. Xu, and T.-K. Yeh, "Metrology assessment of the accuracy of precipitable water vapor estimates from GPS data acquisition in tropical areas: The Tahiti case," *Remote Sens.*, vol. 10, no. 5, p. 758, May 2018.

[6] G. Tagliaferro, A. Gatti, and E. Realini, "Assessment of GNSS zenith total delay estimation using smart devices," in *Proc. 32nd Int. Tech. Meeting Satell. Division Inst. Navigat. (ION GNSS+)*, Oct. 2019, pp. 3879–3891.

[7] M. Kačmařík *et al.*, "Inter-technique validation of tropospheric slant total delays," *Atmos. Meas. Techn.*, vol. 10, no. 6, pp. 2183–2208, Jun. 2017.

[8] J. W. Marini, "Correction of satellite tracking data for an arbitrary tropospheric profile," *Radio Sci.*, vol. 7, no. 2, pp. 223–231, Feb. 1972.

[9] D. Landskron and J. Böhm, "VMF3/GPT3: Refined discrete and empirical troposphere mapping functions," *J. Geodesy*, vol. 92, no. 4, pp. 349–360, Apr. 2018.

[10] J. L. Davis, T. A. Herring, I. I. Shapiro, A. E. E. Rogers, and G. Elgered, "Geodesy by radio interferometry: Effects of atmospheric modeling errors on estimates of baseline length," *Radio Sci.*, vol. 20, no. 6, pp. 1593–1607, Nov. 1985.

[11] N. Zernov and B. Lundborg, "The statistical theory of wave propagation and HF propagation in the ionosphere with local inhomogeneities," Swedish Inst. Space Physics, Kiruna, Sweden, IRF Sci. Rep. 215, 1993.

[12] D. Perler, A. Geiger, and F. Hurter, "4D GPS water vapor tomography: New parameterized approaches," *J. Geodesy*, vol. 85, no. 8, pp. 539–550, Aug. 2011.

[13] Z. Dong and S. Jin, "3-D water vapor tomography in Wuhan from GPS, BDS and GLONASS observations," *Remote Sens.*, vol. 10, no. 2, p. 62, Jan. 2018.

[14] R. Notarpietro, M. Cucca, M. Gabella, G. Venuti, and G. Perona, "Tomographic reconstruction of wet and total refractivity fields from GNSS receiver networks," *Adv. Space Res.*, vol. 47, no. 5, pp. 898–912, Mar. 2011.

[15] K. Hirahara, "Local GPS tropospheric tomography," *Earth, Planets Space*, vol. 52, no. 11, pp. 935–939, Nov. 2000.

[16] A. Flores, G. Ruffini, and A. Rius, "4D tropospheric tomography using GPS slant wet delays," *Annales Geophysicae*, vol. 18, no. 2, pp. 223–234, 2000.

[17] M. Bender, R. Stosius, F. Zus, G. Dick, J. Wickert, and A. Raabe, "GNSS water vapour tomography—Expected improvements by combining GPS, GLONASS and Galileo observations," *Adv. Space Res.*, vol. 47, no. 5, pp. 886–897, Mar. 2011.

[18] W. Rohm, K. Zhang, and J. Bosy, "Limited constraint, robust Kalman filtering for GNSS troposphere tomography," *Atmos. Meas. Techn.*, vol. 7, no. 5, pp. 1475–1486, May 2014.

[19] B. Zhang, Q. Fan, Y. Yao, C. Xu, and X. Li, "An improved tomography approach based on adaptive smoothing and ground meteorological observations," *Remote Sens.*, vol. 9, no. 9, p. 886, Aug. 2017.

[20] H. W. Janes, R. B. Langley, and S. P. Newby, "Analysis of tropospheric delay prediction models: Comparisons with ray-tracing and implications for GPS relative positioning," *Bull. Géodésique*, vol. 65, no. 3, pp. 151–161, Sep. 1991.

[21] J. L. Awange, *Environmental Monitoring using GNSS: Global Navigation Satellite Systems*. Berlin, Germany: Springer, 2012.

[22] A. Angrisano, S. Gaglione, C. Gioia, M. Massaro, and S. Troisi, "Benefit of the NeQuick Galileo version in GNSS single-point positioning," *Int. J. Navigat. Observ.*, vol. 2013, pp. 1–11, Nov. 2013.

[23] Z. Deng et al., "Validation of tropospheric slant path delays derived from single and dual frequency GPS receivers," *Radio Sci.*, vol. 46, no. 6, pp. 1–11, Dec. 2011.

[24] Z. Deng, "GPS meteorology with single frequency receivers," GFZ German Res. Centre Geosci., Potsdam, Germany, Sci. Tech. Rep. STR12/09, 2012.

[25] G. D. Thayer, "An improved equation for the radio refractive index of air," *Radio Sci.*, vol. 9, no. 10, pp. 803–807, Oct. 1974.

[26] M. Boccolari et al., "GPS zenith total delays and precipitable water in comparison with special meteorological observations in Verona (Italy) during MAP-SOP," *Ann. Geophys.*, vol. 45, no. 5, pp. 599–608, 2002.

[27] L. Pheulpin, A. Recking, L. Sichoix, and J.-P. Barriot, "Extreme floods regionalisation in the tropical island of Tahiti, French polynesia," in *Proc. E3S Web Conf.*, vol. 7, 2016, p. 01014.

[28] R. Dach, S. Lutz, P. Walser, and P. Fridez, Eds., *Bernese GNSS Software Version 5.2*. Bern, Switzerland: Univ. of Bern, Bern Open Publishing, 2015.

[29] J. Kouba, "A guide to using international GNSS service (IGS) products," *Geod. Surv. Division Nat. Resour. Canada Ottawa*, vol. 6, p. 34, 2009.

[30] J. Saastamoinen, "Contributions to the theory of atmospheric refraction," *Bull. géodésique*, vol. 105, no. 1, pp. 279–298, Sep. 1972.

[31] F. Zhang, P. Feng, J. Barriot, M. Hopuare, and L. Sichoix, "Correlation between integrated precipitable water vapor and precipitable water during the heavy rainfall event of February 2018 in the Tahiti Island (South Pacific)," in *Proc. Int. Conf. Earth Observat. Societal Impacts (ICEO&SI)*, Hsinchu, Taiwan, Jul. 2018, pp. 1–4.

[32] C. Lu et al., "Real-time retrieval of precipitable water vapor from GPS and BeiDou observations," *J. Geodesy*, vol. 89, no. 9, pp. 843–856, Sep. 2015.

[33] S. Abdel-Monam Younes, "Evaluation of wet mapping functions used in modeling tropospheric propagation delay effect on GPS measurements," *Open Atmos. Sci. J.*, vol. 11, no. 1, pp. 1–15, May 2017.

[34] J. Moffett, "Program requirements for two-minute integrated Doppler satellite navigation solution," Appl. Phys. Lab., Johns Hopkins Univ., Baltimore, MD, USA, Tech. Memorandum TG 819-1, 1973.

[35] J. Boehm, "Vienna mapping functions in VLBI analyses," *Geophys. Res. Lett.*, vol. 31, no. 1, 2004, Art. no. L01603.

[36] J. Tu, D. Gu, Y. Wu, and D. Yi, "Phase residual estimations for PCVs of spaceborne GPS receiver antenna and their impacts on precise orbit determination of GRACE satellites," *Chin. J. Aeronaut.*, vol. 25, no. 4, pp. 631–639, Aug. 2012.

[37] Y. Shoji et al., "Tsukuba GPS dense net campaign observation: Improvement in GPS analysis of slant path delay by stacking one-way post-fit phase residuals," *J. Meteorological Soc. Jpn.*, vol. 82, no. 1B, pp. 301–314, 2004.

[38] K.-D. Park, R. S. Nerem, M. S. Schenewerk, and J. L. Davis, "Site-specific multipath characteristics of global IGS and CORS GPS sites," *J. Geodesy*, vol. 77, no. 12, pp. 799–803, Jun. 2004.

[39] C. Alber, R. Ware, C. Rocken, and J. Braun, "Obtaining single path phase delays from GPS double differences," *Geophys. Res. Lett.*, vol. 27, no. 17, pp. 2661–2664, Sep. 2000.

[40] Y.-M. Bi, J.-T. Mao, X.-Y. Liu, Y. Fu, and C.-C. Li, "Remote sensing of atmospheric integrated water vapor along slant paths using ground based GPS," *Chin. J. Geophys.*, vol. 49, no. 2, pp. 282–290, Mar. 2006.

[41] P. Hordyniec, J. Kapłon, W. Rohm, and M. Kryza, "Residuals of tropospheric delays from GNSS data and ray-tracing as a potential indicator of rain and clouds," *Remote Sens.*, vol. 10, no. 12, p. 1917, 2018.

[42] P. Elosegui and J. Davis, "Accuracy assessment of GPS slant-path determinations," Tsukuba, Japan, Tech. Rep., 2003.

[43] J. L. Davis, G. Elgered, A. E. Niell, and C. E. Kuehn, "Ground-based measurement of gradients in the 'wet' radio refractivity of air," *Radio Sci.*, vol. 28, no. 6, pp. 1003–1018, Nov. 1993.

[44] X. Li et al., "Retrieving high-resolution tropospheric gradients from multiconstellation GNSS observations," *Geophys. Res. Lett.*, vol. 42, no. 10, pp. 4173–4181, May 2015.

[45] R. N. Treuhaft and G. E. Lanyi, "The effect of the dynamic wet troposphere on radio interferometric measurements," *Radio Sci.*, vol. 22, no. 2, pp. 251–265, Mar. 1987.

[46] S. Schön and F. K. Brunner, "A proposal for modelling physical correlations of GPS phase observations," *J. Geodesy*, vol. 82, no. 10, pp. 601–612, Oct. 2008.

[47] M. Vennebusch, S. Schön, and U. Weinbach, "Temporal and spatial stochastic behaviour of high-frequency slant tropospheric delays from simulations and real GPS data," *Adv. Space Res.*, vol. 47, no. 10, pp. 1681–1690, May 2011.

[48] A. D. Wheelon, *Electromagnetic Scintillation I. Geometrical Optics*. Cambridge, U.K.: Cambridge Univ. Press, 2001.

[49] H. W. Ellsaesser, "Expansion of hemispheric meteorological data in antisymmetric surface spherical harmonic (Laplace) series," *J. Appl. Meteorol.*, vol. 5, no. 3, pp. 263–276, Jun. 1966.

[50] P. Gautron, J. Krivanek, S. Pattanaik, and K. Bouatouch, "A novel hemispherical basis for accurate and efficient rendering," in *Proc. 15th Eurograph. Conf. Rendering Techn. (EGSR)*, 2004, pp. 321–330.

[51] H. Huang et al., "Hemispherical harmonic surface description and applications to medical image analysis," in *Proc. 3rd Int. Symp. 3D Data Process., Vis., Transmiss.*, Jun. 2006, pp. 381–388.

[52] W. A. Heiskanen and H. Moritz, *Physical Geodesy*. San Francisco, CA, USA: Freeman, May 1967, pp. 1–364.

[53] H. Moritz, "Covariance functions in least-squares collocation," Dept. Geodetic Sci., Ohio State Univ., Columbus, OH, USA, Tech. Rep. 240, 1976.

[54] A. N. Kolmogorov, "The local structure of turbulence in incompressible viscous fluid for very large Reynolds numbers," *Dokl. Akad. Nauk SSSR*, vol. 30, pp. 301–305, 1941.

[55] V. I. Tatarski, *Wave Propagation in a Turbulent Medium*. New York, NY, USA: McGraw-Hill, New York, 1961.

[56] G. Matheron, *Traité de géostatistique appliquée*. Paris, France: Éditions Technip, 1962.

[57] E. O. Schulz-DuBois and I. Rehberg, "Structure function in lieu of correlation function," *Appl. Phys.*, vol. 24, no. 4, pp. 323–329, Apr. 1981.

[58] A. H. Dodson, P. J. Shardlow, L. C. M. Hubbard, G. Elgered, and P. O. J. Jarlemark, "Wet tropospheric effects on precise relative GPS height determination," *J. Geodesy*, vol. 70, no. 4, pp. 188–202, Jan. 1996.

[59] C. S. Ruf and S. E. Beus, "Retrieval of tropospheric water vapor scale height from horizontal turbulence structure," *IEEE Trans. Geosci. Remote Sens.*, vol. 35, no. 2, pp. 203–211, Mar. 1997.

[60] G. M. Jenkins and D. G. Watts, *Spectral Analysis and Its Applications*. San Francisco, CA, USA: Holden Day, 1968.

[61] A. Broman, *Introduction to Partial Differential Equations: From Fourier Series to Boundary-value Problems*. Reading, MA, USA: Addison-Wesley, 2010.

[62] J. P. Boyd, *Chebyshev and Fourier Spectral Methods*. New York, NY, USA: Dover, 2010.

[63] D. B. Percival and A. T. Walden, *Wavelet Methods for Time Series Analysis*. Cambridge, U.K.: Cambridge Univ. Press, 2009.

[64] I. Daubechies, *Ten Lectures on Wavelets, CBMS-NSF Regional Conference Series in Applied Mathematics*, vol. 61. Philadelphia, PA, USA: SIAM, 1992, pp. xix and 357.

[65] E. A. Barnes and D. L. Hartmann, "The global distribution of atmospheric eddy length scales," *J. Climate*, vol. 25, no. 9, pp. 3409–3416, May 2012.

[66] V. Laurent, K. Maatuaiahutapu, J. Maiau, and P. Varney, *Atlas climatologique de la Polynésie Française*. Paris, France: Météo-France, Direction Interrégionale de Polynésie Française, Puna'auia, 2004.

[67] B. Y. E. Bar-Sever et al., "Atmospheric media calibration for the deep space network,"*Proc. IEEE* vol. 95, no. 11, pp. 2180–2192, Nov. 2007.

[68] C. W. Higgins, M. Froidevaux, V. Simeonov, N. Vercauteren, C. Barry, and M. B. Parlange, "The effect of scale on the applicability of Taylor's frozen turbulence hypothesis in the atmospheric boundary layer," *Boundary-Layer Meteorol.*, vol. 143, no. 2, pp. 379–391, May 2012.

Fangzhao Zhang (Student Member, IEEE) received the master's degree from the Institute of Geodesy and Geophysics, UCAS, Wuhan, China, in 2016, and the Ph.D. degree from the University of French Polynesia, Faaa, French Polynesia, in January 2020.

Her research interest includes the study of the determination of precipitable water vapor (PWV) based on GNSS techniques and its application on meteorology.

Jean-Pierre Barriot received the Ph.D. degree in theoretical physics from the University of Montpellier, Montpellier, France, in 1987, and the Habilitation degree in space physics from the University of Toulouse, Toulouse, France, in 1997.

Since 2006, he has been a Distinguished Professor of geophysics with the University of French Polynesia, Faaa, French Polynesia, and the Head of the Geodesy Observatory of Tahiti, a joint Geodetic Observatory of CNES, NASA, and UPF. He is also an Invited Professor with the University of Wuhan, Wuhan, China. His research areas range from geophysics of the Earth and planets, Earth and planetary atmospheres, and orbitography.

Guochang Xu is a former Long-Term Senior Scientist with GeoForschungs-Zentrum-Potsdam, Potsdam, Germany. He is with the Harbin Institute of Technology of Shenzhen, Shenzhen, China. His research areas range from satellite navigation, remote sensing, and celestial mechanics.

Marania Hopuare received the Ph.D. degree in atmospheric physics from the University of French Polynesia (UPF), Faaa, French Polynesia, in 2014.

She is an Assistant Professor (Maitre de Conférences) with UPF. Her studies range from atmospheric physics to tropical climatology, including the relationship between renewable energies and climate.